Structure and low temperature micromechanical properties of as-cast and SPD-processed high-entropy $Co_{25-x}Cr_{25}Fe_{25}Ni_{25}C_x$ alloys

A.V. Levenets[1], H.V. Rusakova[2], L.S. Fomenko[2], Yi Huang[3,4], I.V. Kolodiy[1], R.L. Vasilenko[1], E.D. Tabachnikova[2], M.A. Tikhonovsky[1], T.G. Langdon[4]

[1]National Science Center "Kharkov Institute of Physics and Technology" of the National Academy of Sciences of Ukraine, Kharkiv 61108, Ukraine

[2]B.Verkin Institute for Low Temperature Physics and Engineering of the National Academy of Sciences of Ukraine, Kharkiv 61103, Ukraine

3Department of Design and Engineering, Faculty of Science and Technology, Bournemouth University, Poole, Dorset BH12 5BB, UK

[4]Department of Mechanical Engineering, University of Southampton, Southampton, SO17 1BJ, UK

E-mail: a.levenets@kipt.kharkov.ua

The effect of carbon additions on the structure and mechanical properties of high-entropy alloys $Co_{25-x}Cr_{25}Fe_{25}Ni_{25}C_x$ (x = 0, 1, 3, at. %) in two structural states, as-cast coarse-grained (CG) samples and nanocrystalline (NC) obtained by severe plastic deformation (SPD), was studied. The SPD was performed by high-pressure torsion at room temperature. The mechanical properties were investigated by microindentation in the temperature range of T = 77-300 K. It was found that in the as-cast state, all alloys had a dendritic microstructure and an inhomogeneous distribution of elements. At x = 0 and x = 1, the dendrites were enriched in iron and nickel, and the interdendrite regions were enriched in chromium. At x = 3, in the interdendrite regions, a eutectic consisting of a multicomponent matrix and fine eutectic dendrites of M_7C_3 carbide, where M is predominantly chromium, was formed. The main phase in alloys had an fcc lattice, while the solubility of carbon in it was about 1 at. %. SPD led to effective refinement of the microstructure (the size of the coherent scattering regions was about 30-50 nm), to an increase in the dislocation density up to $(1\text{-}1.5)\times10^{15}$ m^{-2} and to an increase in the concentration of stacking faults. The microhardness of CG alloys at room temperature increased monotonically with increasing carbon concentration, while in NC alloys the maximum microhardness H_V was achieved at 1 at. % of carbon. The reason for this anomalous behavior of the microhardness of NC alloys is an increase in the grain size and a decrease in the dislocation density in the alloy with x = 3 compared to the alloy with x = 1. As the temperature decreased from room temperature to the temperature of liquid nitrogen, the microhardness of CG and NC alloys increased by about 1.5-1.7 and 1.2-1.5 times, respectively, which indicates the thermally-activated nature of plastic deformation under the indenter. The results obtained indicate that the main role in the hardening of the CG alloys $Co_{25-x}Cr_{25}Fe_{25}Ni_{25}C_x$ is due to solid solution and dispersion hardening, while in NC alloys it is hardening due to a decrease in the grain size (according to the Hall-Petch relation) and an increase in the dislocation density (according to the Taylor relation).

Keywords: high-entropy alloys, carbon alloying, microstructure, microhardness, severe plastic deformation, deformation mechanisms.

1. Introduction

Currently, there is a new actively developed class of materials named high entropy (HEA) or, in a broader formulation, multicomponent alloys (MCA), multiprincipal alloys (MPA) or complex concentrated alloys (CCA) [1-4], as proposed by Yeh et al. [5] and Cantor et al. [6] in 2004. These alloys contain 4-5 and more components in equiatomic or near-equiatomic concentration. The consequence of such composition is the absence of a "base" metal and an increased value of the mixing entropy (configurational entropy) compared to "traditional" alloys. A high mixing entropy value leads to a decreased Gibb's free energy, which stabilizes a disordered solid solution state with simple fcc or bcc lattices [1, 3, 4]. The presence of dissimilar atoms with different radii and electron shell in such solutions causes significant lattice distortions, where these are one of the factors providing the unique mechanical properties of HEA [7-10]. It is expected [11] that due to these properties HEA can be widely used in various fields of technology, such as aerospace [12, 13], nuclear power [4, 14], cryogenics [15], biomedicine [16], etc. It should be noted that HEA with bcc lattices predominantly possess high strength characteristics with medium or low plasticity [9-12], whereas HEA with fcc lattices have outstanding plasticity at relatively low strength characteristics [7-10]. This applies to various five- and four-component (and even three-component) fcc alloys of the Co-Cr-Fe-Mn-Ni system. It is especially important that these alloys have a high ductility at low temperatures (down to 0.5 K [17-19]), as well as a record fracture toughness in the cryogenic region [15]. Obviously, it is desirable to increase the strength properties, primarily the yield strength, while maintaining good plasticity and fracture toughness for the future wide practical application of HEA.

The equiatomic $Co_{20}Cr_{20}Fe_{20}Mn_{20}Ni_{20}$ alloy (the composition is in at. %), called the Cantor alloy [6, 20], is the most studied alloy of the above-mentioned system. Various materials science approaches were used to increase the strength characteristics of this alloy such as deformation by rolling at 77 K [21], alloying with metals forming hard intermetallic compounds in the alloy [8, 22-25], alloying with interstitial elements, primarily carbon, in combination with thermomechanical treatments [26, 27] and creation of a nanostructured state by severe plastic deformation methods (SPD) [28-30]. The implementation of these approaches has led to a number of positive results. Thus, 1 at. % C introduction into the alloys in combination with rolling and annealing at 800 ºC [26] increased the yield strength of the Cantor alloy at room temperature by more than 2 times while maintaining high plasticity (elongation to fracture 37 %). Severe plastic deformation of the Co-Cr-Fe-Mn-Ni alloys by high pressure torsion (HPT) has led to a significant increase in their strength characteristics [28-30]. For instance, HPT of the

$Co_{20}Cr_{26}Fe_{20}Mn_{20}Ni_{14}$ alloy at room temperature increased the ultimate strength by three times (from 700 to 2100 MPa) with an elongation to fracture of 5 % [30].

Further studies of fcc HEA have shown that the mechanical properties of the four-component equiatomic CoCrFeNi alloy are not only no worse, but they are even better than the Cantor alloy properties, especially at cryogenic temperatures, although the yield strength does not always satisfy the existing requirements. Therefore, as in the case of the Cantor alloy, attempts were made to strengthen the CoCrFeNi alloy by various methods, in particular through carbon alloying [31-33]. It was established, that carbon increases the strength characteristics of a coarse-crystalline alloy both through solid-solution strengthening by carbon atoms and precipitation hardening by the resulting carbides.

It is of great interest to study the combined effect of two factors, namely alloying and severe plastic deformation, on the structure and mechanical properties of the CoCrFeNi alloy. The aim of this work was therefore to study the effect of carbon alloying on the structure and microhardness of $Co_{25-x}Cr_{25}Fe_{25}Ni_{25}C_x$ alloys at T = 77 – 300 K in a cast coarse-grained and nanostructured state obtained by SPD. The SPD was carried out by the HPT method, which produces the large shear deformations and is the most effective way to create the nanostructured state. A microindentation method was used to study the mechanical properties where this is the most convenient for studying the samples with heterogeneous structure after HPT. This method provides a large number of measurements on a small surface of the same sample and permits data based on good statistics [28-30, 34, 35].

It must be noted that carbon was added by reducing the corresponding amount of cobalt in $Co_{25-x}Cr_{25}Fe_{25}Ni_{25}C_x$, contrary to a number of studies [26, 27, 31-33], in which carbon was an addition to the equiatomic composition, i.e., $Co_{25}Cr_{25}Fe_{25}Ni_{25}C_x$. This was necessary because, according to several studies [36, 37], carbon atoms dissolved in the fcc lattice of the Co-Cr-Fe-Mn-Ni HEA system increase the stacking fault energy (SFE). A decrease in the cobalt concentration in the alloys with fcc lattice acts in the same way [38]. The SFE increase can lead to a change of deformation mechanism of the material and, thus, affect the properties.

2. Materials and methods

2.1. Sample processing

Metals with a purity of at least 99.9 % and spectrally pure graphite were used for the alloy melting. Ingots weighing 20 g with various carbon content x = 0; 1; 3 (indicated in at. %) were obtained by arc melting in a copper mold using a non-consumable tungsten electrode. To ensure the chemical homogeneity, the ingots were flipped over and remelted at least 5 times [22,

26, 27]. At the final stage, the melt was poured into a massive copper cylinder with an inner diameter of 10 mm. Disks with a diameter of 10 mm and a thickness $h \approx 1.1$ mm were obtained from cylindrical rods by spark cutting. The disks were sanded on both sides on 400-2000 grit abrasive paper so that the final disk thickness was $h \approx 0.9$ mm. SPD was performed by HPT at room temperature to obtain a nanostructured state [35]. The plunger was rotated at a rate of 0.7 rpm under a hydrostatic pressure of 6 GPa. During torsion, the magnitude of the shear strain γ depends on the distance from the rotation axis r and can be calculated by the equation

$$\gamma = 2\pi Nr/h, \quad (1)$$

where N is the number of revolutions and h is the thickness of the disk [39].

Various degrees of plastic deformation were obtained by changing the number of revolutions N from $N = 1$ to $N = 5$. In total, 9 types of samples were studied, marked further as CxNy, where x denotes the content of carbon in at. % for each alloy and y denotes the number of revolutions during HPT. For example, C3N1 corresponds to the alloy containing 3 at. % of carbon and subjected to 1 revolution ($N = 1$).

2.2. Structure investigations

The microstructure of as-cast samples was studied on a plane perpendicular to the axis of the disks using a metallographic inversion microscope Olympus GX51 and a scanning electron microscope JSM 7001F equipped with a system for energy-dispersive X-ray spectroscopy (EDS) INCA ENERGY 350. Before the study the plane was mechanically ground and a final mirror-smooth surface was obtained by polishing on a soft tissue using a paste based on chromium oxide. To reveal the microstructure, a freshly prepared etchant was used, consisting of 5 parts of CH_3COOH, 3 parts of HNO_3, 1 part of H_2PO_4, 1 part of H_2SO_4, and 1 part of HCl.

X-ray studies of as-cast and HPT-processed specimens were carried out on thin sections prepared by a similar method, but not subjected to etching. XRD analysis was performed using a DRON-4-07 diffractometer in Cu-Kα radiation using a selectively absorbing filter. Standard processing (background removing, $K\alpha_2$ reduction, diffraction peaks fitting by pseudo-Voigt function) was applied for all diffraction patterns to obtain the peak characteristics (diffraction angle 2θ, integral intensity I, integral breadth B, interplanar spacing d) needed for further calculations. A microstructural study was performed using the integral breadth analysis method. Separated values of coherent-scattering domain (CSD) sizes and microstrains were obtained using a Williamson-Hall plot. The main operational formula of this method is [40]:

$$\beta = \frac{\lambda}{D\cos(\theta)} + 4\varepsilon\mathrm{tg}(\theta), \quad (2)$$

where β is the physical peak broadening (experimentally observed broadening corrected for instrumental broadening); λ is the radiation wavelength; D is the crystallite size; ε is the microstrain value and θ is the diffraction angle. Annealed silicon powder was used as a standard specimen for instrumental correction. Based on the obtained size-strain characteristics, the dislocation density was estimated from the equation [41]:

$$\rho = \frac{3\sqrt{2\pi\varepsilon}}{Db}, \quad (3)$$

where ρ is the dislocation density, b is the Burgers vector ($b = \frac{1}{2} < 110 > = \frac{a\sqrt{2}}{2}$ for fcc crystals).

2.3. *Microhardness measurements*

The microhardness was measured in the temperature range of 77 – 300 K on the same thin sections on which X-ray structural analysis was carried out. At room temperature a PMT-microhardness tester was used, and at lower temperatures, a special low-temperature device with a freely suspended Vickers pyramid was used [42]. At T = 77 K the sample and the indenter were in liquid nitrogen, and at higher temperatures they were in the vapor of cooled gaseous nitrogen. The load on the indenter was varied in the range P = 0.1 - 2.2 N and the loading duration was t = 10 s.

Microhardness was calculated by the relation: $H_V = 1{,}854P/(2a)^2$, where $2a$ is the length of the indentation diagonal. In this work, the dependences of the microhardness on the indentation load $H_V(P)$, on the distance from the disk center $H_V(r)$ and on the temperature $H_V(T)$ were investigated. With the dependences $H_V(P)$ and $H_V(T)$, each point corresponds to the average value of the microhardness, calculated from 10 indentations. With the dependences H_V each point corresponds to one indentation (local microhardness). Note that all the measuring results $H_V(T)$ for specimens subjected to HPT were obtained by indenting homogeneous areas adjacent to the disk edge.

3. Experimental results and discussion

3.1. Alloy structure

Coarse-grained (CG) alloys. Based on an examination of the as-cast alloys with different carbon contents, all alloys are coarse-grained with grain sizes of several hundred micrometers and have dendritic structures (Fig. 1) but the degree of dendritic development differs. In the

absence of carbon (sample C0N0), there are no first-order branches in the dendrites [Fig. 1(a)], and the alloy has a columnar (cellular) microstructure. The reason for the formation of such structure is the variation of the partition coefficient k from 1 [43]. Elements with $k < 1$ at the crystallization front are pushed into the melt, and constitutional undercooling occurs at the front (the macroscopic crystallization front is perpendicular to the plane of Fig. 1(a)), so that the plane front at the microscopic level loses its stability and breaks up into cells. As a result, a nonuniform distribution of elements is observed in the crystallized alloy. EDS mapping showed that nickel is distributed almost uniformly through the alloy, while iron and cobalt are located mostly in dendrites (D), and chromium is predominantly in the interdendritic regions (ID) (Fig. 2). Nevertheless, the difference between their concentration in dendrites and interdendritic regions is small and it does not exceed several atomic percent (Table 1).

Adding of 1 at. % C into the alloy (sample C1N0) increases the degree of supercooling at the crystallization front (the carbon distribution coefficient in all the metals contained in the alloy is $k < 1$, therefore carbon accumulates in liquid ahead of the crystallization front), and the microstructure changes from columnar to more developed dendritic [Fig. 1(b)]. According to microanalysis, the distribution of metallic elements in the alloy does not qualitatively change (Table 1): thus, interdendritic regions and grain boundaries are enriched with chromium and carbon, and the carbon concentration is sufficient for the single carbide formation in some local areas [Fig. 1(b)]. Local composition microanalysis showed that the largest carbide [Fig. 1(b), insert] contains 41.68 % C, 35.44 % Cr, 9.28 % Fe and 5.70 % Ni. This composition approximately corresponds to the M_7C_3 carbide (taking into account the overestimation of the carbon concentration in the used technique) with chromium as the main metal component. Based on the very small volume fraction of the detected carbides, it can be assumed that almost all carbon is dissolved in the matrix so that its solubility is close to 1 at. %. An increase of the carbon concentration up to 3 at. % (sample C3N0) leads to further carbon and chromium enrichment in the interdendritic regions (Fig. 3). As a result, a eutectic is formed in the interdendritic regions [Figs. 1(c) and 1(d)] and this was previously observed in five- and four-component high-entropy alloys containing carbon [33, 35, 44]. Herewith, the eutectic contains a multicomponent matrix phase and thinly branched dendrites (microdendrites) of carbide M_7C_3, with M – chromium mainly [44, 35, 33]. The elemental concentration in the interdendritic eutectic differs significantly from the composition of the interdendritic regions in the C0N0 and C1N0 alloys. Thus, the eutectic is highly enriched with chromium, and depleted with cobalt, iron, and nickel (Table 1, Fig. 3). The eutectic has a rod morphology, which is typical for a system in which the volume fraction of the second phase (carbide, in this case) is less than 30 % [43]. The diameter of the carbide rods is approximately 0.1 μm [Fig. 1(d)].

The diffraction patterns of all as-cast CG alloys are very close to each other and show the presence of only one fcc phase. As an example, Figure 4 shows a diffraction pattern of the as-cast alloy containing 3 at. % C (sample C3N0). The volume fraction of the carbide phase, detected with microscopic studies [Figs. 1(c) and 1(d)], is apparently below the sensitivity limit of the X-ray method and therefore it is less than 5 %. Processing of the diffraction patterns showed that the fcc lattice parameters of the C0N0, C1N0 and C3N0 alloys are 3.577 Å, 3.583 Å and 3.585 Å, respectively (±0.001 Å). The increase in lattice parameter of C1N0 in comparison with the C0N0 alloy confirms the presence of carbon solubility in the alloy and the formation of an interstitial solid solution. Moreover, the almost equality of the C1N0 and C3N0 parameters means that the carbon solubility limit does not exceed 1 at. % in the rapidly crystallised alloy. This conclusion is in accordance with the metallographic results presented above and literature data [26, 27, 33]. Note that the increase in lattice parameter of C1N0 in comparison with the C0N0 alloy is about 0.006 Å, which is close to the 0.0068 value, presented in [33]. Carbon, not included in the solid solution in C3N0 alloy, is concentrated in the eutectic and forms the eutectic carbide M_7C_3 with tetragonal lattice [26, 33, 44].

Nanocrystalline (NC) alloys. The diffraction patterns of the alloys after HPT are also similar to each other. As an example, Figure 4(b) shows the diffraction pattern of the alloy containing 3 at. % C, subjected to one HPT revolution (sample C3N1). After SPD, the phase compositions of the alloys does not change (according to the applied method) and all the samples have fcc lattice and <111> texture. Nevertheless, all the diffraction patterns of the deformed specimens show shifting of the diffraction peaks. It is known that such a shift occurs in the presence of stacking faults (SF). In particular, the (200) peaks shift toward smaller angles, and the (111) peaks – toward larger angles for the fcc crystals. In this regard, lattice parameters of the fcc phase of the deformed alloys were calculated from the (311) peak, since it shifts less than others due to the presence of SF and it is observed near the precise region of 2θ angles. The stacking fault concentration (SFC) α was estimated from the distance change between (111) and (200) peaks according to the following equations [45]:

$$\Delta 2\theta^\circ = -\frac{4\sqrt[5]{3}\alpha}{\pi^2}\left(\tan\theta_{200} + \frac{1}{2}\tan\theta_{111}\right), \quad (4)$$

$$\Delta 2\theta^\circ = (2\theta_{200} - 2\theta_{111})_{\text{def}} - (2\theta_{200} - 2\theta_{111})_{\text{ann}}. \quad (5)$$

It can be seen from eq. (4) that the angular positions of the (111) and (200) peaks of deformed and annealed samples are required for the calculation. Since the samples in the annealed state were not investigated, the corresponding values were calculated based on the experimentally determined lattice parameters. Certainly, this approach introduces some inaccuracy, but it is

sufficient for a semi-quantitative assessment. The calculated lattice parameters and substructural parameters are presented in Table 2.

Note that the minimum crystallite size, maximum values of the dislocation density and the stacking fault concentration are observed in the alloy doped with 1 at. % C (C1N1). The crystallite size increase in the alloy doped with 3 at. % C (C3N1) may be due to the presence of relatively large and hard carbide particles that prevent grain refinement during SPD as observed earlier in [35].

3.2. Microhardness of alloys in the temperature range of 77 – 300 K

This section presents the results of studying of the effect of indentation load, the magnitude of shear strain during torsion and temperature on the microhardness of $Co_{25-x}Cr_{25}Fe_{25}Ni_{25}C_x$ (x = 0; 1; 3) alloys.

3.2.1. Effect of indentation load. A study of the $H_V(P)$ dependence showed that the effect of indentation load weakened with increasing carbon concentration in the CG samples (Fig. 5). Specifically, the microhardness of the pure alloy (C0N0 sample) increased by 1.5 times with the indentation load decreasing from P = 2.2 N to P = 0.1 N. The H_V increase in the alloy with 1 at. % C (C1N0 sample) was about 14 %, while the H_V value in the alloy with x = 3 (C3N0 sample) was almost unchanged over the entire load range. Probably, the reason for the different nature of the $H_V(P)$ dependences is the different ability of these materials to accumulate defects in the near-surface layer during mechanical grinding but this requires additional study. For all the studied alloys (x = 0, 1, 3) the microhardness weakly depended on the load value in the $P \geq 1.5$ N region (Fig. 5). The microhardness values in this region of load are called «true microhardness» since it is believed that they reflect the microhardness not of the surface layer, but of the sample volume. The obtained data made it possible to choose the optimal indentation load of $P \geq 1.5$ N for further studies, since the effect of load on the microhardness could be neglected.

3.2.2. Effect of the magnitude of shear strain during torsion. Microhardness is a structure-sensitive value that is often used to quantify the inhomogeneity of the structural state of samples subjected to HPT. At room temperature we measured the microhardness depending on the distance from the disk center r (Fig. 6) for N = 1. Each point in Fig. 6 corresponds to the microhardness value calculated from one indentation, so that Figure 6 gives information not only about the change in H_V with an increase in the distance from the center of the disk, but also about the absolute spread of the microhardness values relative to the average value. It is seen that

significant changes in the microhardness with r were observed in the central part of the disk. Closer to the periphery (at distances less than about 2 mm from the circle bounding the disk), the microhardness remained practically unchanged (within the scatter) and this indicates a sufficient homogeneity of the microstructure of this area. This was the area of the disk that was subsequently used to study the effect of temperature on microhardness. From Fig. 6 it is seen that an increase in the carbon concentration up to 1 at. % (x = 1) is accompanied by a remarkable increase in microhardness. At the same time, a further increase in the carbon concentration to 3 at. % (x = 3) led to an unexpected drop in microhardness to the level of the sample with x = 0 or even lower. Note that, for CG specimens of $Co_{25-x}Cr_{25}Fe_{25}Ni_{25}C_x$ alloys which were not subjected to torsion, a monotonic increase in microhardness was observed with an increase in carbon concentration (see Fig. 5). So, apparently, it is the torsional deformation that led to the observed anomalous change in the microhardness. Possible reasons for this anomaly are discussed below. One of the two branches $H_V(r)$ in Fig. 6 with smaller scatter of points was presented for each of the studied alloys in the coordinates $H_V(\gamma)$ in Fig. 7, where shear deformation γ is defined according to eq. (1). It can be seen that the $H_V(\gamma)$ dependences significantly weaken as the shear strain increases to γ = 25-30.

3.2.3. Effect of test temperature. The temperature dependences of mechanical characteristics, such as yield strength and microhardness, are of particular interest to clarify the mechanism of plastic deformation of a material [46]. The $H_V(T)$ dependences for CG alloys of all concentrations are shown in Fig. 8. It can be seen that a decrease in temperature from 300 K to liquid nitrogen temperature (77 K) leads to a significant increase (approximately 1.5 times) in microhardness for all investigated alloys. This indicates the thermally-activated nature of plastic deformation under the indenter in these alloys. It can be seen from Fig. 8 that the microhardness of CG alloys increases with an increase in the carbon concentration over the entire investigated temperature range. This may be due to the effects of solid solution and dispersion hardening caused by carbon atoms embedded in the lattice and precipitation of carbides, respectively. Interstitial atoms and carbide particles, being obstacles for moving dislocations, cause an increase in the yield strength [26, 27] and the microhardness at all temperatures. For nanocrystalline (NC) samples obtained by torsion under high pressure, an increase in microhardness (by a factor of 1.2–1.5) is also observed with temperature decrease (Fig. 9), which indicates the retention of the thermally-activated nature of plastic deformation for the nanocrystalline state of alloys. However, a qualitative difference between the data shown in Fig. 8 and Fig. 9 should be noted. A nontrivial behaviour of the microhardness was observed with a change in the carbon concentration for NC alloys in the entire temperature range, namely, lower

values of the microhardness for x = 3 in comparison with the microhardness of the alloy with x = 1. We have already noted a similar anomaly when considering the dependences of the microhardness on the distance from the center of the disk subjected to HPT (Fig. 6), when the microhardness of the alloy with x = 3 was lower than of the alloy with x = 1 for all values of *r*. To explain the anomalous effect of the carbon content on H_V, it should be noted that the microhardness of NC samples is several times higher than the microhardness of CG samples where this is a consequence of a significant refinement of grains and an increase in the dislocation density during HPT (see Table 2). The contribution of these two factors exceeds the contribution of solid solution and dispersion hardening and is decisive in the value of the yield stress and microhardness [29, 30]. As can be seen from Table 2, the alloy with 1 at. % C has a minimum crystallite size (averaged over the disk area) and a maximum dislocation density. Note that in NC materials with crystallite sizes less than 50-60 nm, the crystallite sizes practically coincide with the grain size [47]. In addition, a certain contribution to the value of the yield strength is made by the concentration of stacking faults [48], which is also a maximum for the alloy with 1 at. % C (Table 2). Thus, the maximum value of the microhardness in the C1N1 alloy at room temperature (Fig. 6 and Fig. 9) is understandable, as is the approximate equality of the microhardness of the C0N1 and C3N1 samples (Fig. 6), due to the almost identical structural parameters (Table 2). Moreover, the crystallite size in the C3N1 sample turned out to be the largest. A possible reason for the larger crystallite size in the samples with the highest carbon concentration is the presence of solid eutectic carbides in the alloy with x = 3, which prevent grain refinement during torsional deformation [35].

An anomaly associated with the temperature dependence of the microhardness of the C0N1 sample is more difficult to explain, since the microhardness increases more sharply for this alloy than for the others with the temperature decreasing (Fig. 9). The microhardness curves for samples with x = 0 and x = 1 intersect at a temperature of $T \approx 190$ K, and the NC alloy with x = 0 becomes harder than the other alloys at lower temperatures. The reason for this anomalous behaviour of the alloy with x = 0 is probably a “switching on” of an additional deformation mechanism (in addition to dislocation slip) with a decrease in temperature, as with a twinning or phase transformation. It is known [37] that in fcc alloys certain deformation mechanisms depend on the stacking faults energy (SFE): for SFE $\geq$ 40 mJ/m^2 dislocation slip is characteristic, for 40 mJ/m^2 $\geq$ SFE $\geq$ 20 mJ/m^2 there is dislocation slip plus twinning and for 20 mJ/m^2 $\geq$ SFE there is dislocation slip plus a martensitic transformation. It is known from the literature that the experimental values of the SFE for the CoCrFeNi alloy have a significant scatter and, according to a recent study [48], are 18.3 – 40.9 mJ/m^2 at 293 K and 5.3 – 19.8 mJ/m^2 at 140 K, depending on the magnitude of deformation. As can be seen, the SFE strongly decreases with the

temperature decrease and falls into the range of possible deformation by twinning or a phase transformation. Thus, taking into account the high microstrain level in the NC alloy (Table 2), the superposition of internal microstrains and deformation under the indenter may lead to the appearance of nanotwins [49] and this will strengthen the alloy with a decrease in the temperature (the dynamic Hall-Petch effect).

A martensitic transformation can be an alternative since it “turns on” as a result of a decrease in the SFE with a further decrease in the test temperature. At the same time, the SFE is noticeably higher in the studied alloys doped with carbon [36-38], and the "activation" of deformation mechanisms, additional to dislocation slip, may not occur in this temperature range. To confirm these explanations, further experiments are needed on the deformation of alloys at different temperatures under conditions of quasi-static loading and a study of the resultant microstructures using high-resolution electron microscopy.

4. Conclusions

Microstructure, phase composition, substructure parameters and micromechanical properties were studied for $Co_{25-x}Cr_{25}Fe_{25}Ni_{25}C_x$ (x=0; 1; 3) alloys in the as-cast state and after severe plastic deformation by high-pressure torsion (HPT). It was established that:

1. As-cast alloys have a coarse-grained dendritic microstructure with grain sizes of ~ 100 μm. In the absence of carbon (x = 0), the dendritic shape is close to columnar, with the dendrites enriched with chromium and interdendritic regions – with cobalt and iron. Adding of 1 at. % C (x = 1) to the alloy leads to more brunched dendrites without a significant change in the element distribution. With 3 at. % C in the alloy, a eutectic is formed containing a multicomponent matrix enriched with chromium and eutectic microdendrites M_3C_7 (M – chromium, mainly) in the interdendritic regions.

2. Microstructural and X-ray studies showed that the carbon solubility in the as-cast alloys was close to 1 at. %.

3. HPT of the alloys leads to the formation of a nanocrystalline state in the alloys characterized by a small size of coherent scattering regions, high values of microstrains, high values of dislocation density and stacking fault concentrations. Here, the smallest size of crystallites and the largest values of other specified parameters were observed for the alloy doped with 1 at. % C.

4. The microhardness of $Co_{25-x}Cr_{25}Fe_{25}Ni_{25}C_x$ (x = 0, 1, 3) high-entropy alloys in two structural states (as-cast coarse-grained and nanocrystalline after HPT processing at room temperature) was measured in the temperature range of 77-300 K.

5. It is shown that with the temperature decreasing from T = 300 K to T = 77 K, the microhardness of CG and NC alloys increases by approximately 1.5 and 1.3 times, respectively, thereby indicating the thermally-activated nature of plastic deformation under the indenter, regardless of the structural state of the alloys.

6. A nontrivial behaviour of the microhardness of NC alloys was found with an increase in the carbon content. At room temperature, a change in x from 0 to 1 leads to a noticeable increase in H_V (by about 14 %). At the same time, a change in x from 1 to 3 is not accompanied with a further increase in microhardness as observed in CG alloys but leads to a decrease in microhardness approximately to the H_V level of samples with x = 0.

7. The results indicate that solid solution and dispersion hardening play the main role in the strengthening of CG $Co_{25-x}Cr_{25}Fe_{25}Ni_{25}C_x$ (x = 0, 1, 3) alloys. In NC alloys hardening is caused by a decrease in the grain size (according to the Hall-Petch relationship) and increase in the dislocation density (according to the Taylor relationship).

Acknowledgements

AL and MT were supported by the National Research Foundation of Ukraine in frame of the project №2020.02/0327 «Fundamental aspects of the new materials creation with unique physical, mechanical and radiation properties based on the concentrated multicomponent alloys». TGL and YH were supported by the European Research Council under Grant Agreement No. 267464-SPDMETALS.

References

1. D. B. Miracle and O. N. Senkov, *Acta Mater.* **122**, 448 (2017), https://doi.org/10.1016/j.actamat.2016.08.081.
2. E. J. Pickering and N. G. Jones, *Int. Mater. Rev.* **61** 183 (2016), https://doi.org/10.1080/09506608.2016.1180020.
3. E. P. George, D. Raabe, and R. O. Ritchie, *Nat. Rev. Mater.* **4** 515 (2019), https://doi.org/10.1038/s41578-019-0121-4.
4. A. V. Levenets, M. A. Tikhonovsky, V. N. Voyevodin, A. G. Shepelev, and O. V. Nemashkalo, *Problems of atomic science and technology* **2** 3 (2021), http://dx.doi.org/10.46813/2021-132-003.
5. J-W. Yeh, S-K. Chen, S-J. Lin, J-Y. Gan, T-S. Chin, T-T. Shun, C-H. Tsau, and S-Y. Chang, *Adv. Eng. Mater.* **6** 299 (2004), https://doi.org/10.1038/s41578-019-0121-4.
6. B. Cantor, I. T. H. Chang, P. Knight, and A. J. B. Vincent, *Mat. Sci. Eng. A* **375-377** 213 (2004), https://doi.org/10.1016/j.msea.2003.10.257.
7. Z. Li, Sh. Zhao, R. O. Ritchie, and M. A. Meyers, *Prog. Mater. Sci.* **102** 296 (2019), https://doi.org/10.1016/j.pmatsci.2018.12.003.
8. Z. Zeng, M. Xiang, D. Zhang, J. Shi, W. Wang, X. Tang, W. Tang, Y. Wang. X. Ma, Z. Chen, W. Ma, and K. Morita, *J. Mater. Res. and Techn.***15** 1920 (2021), https://doi.org/10.1016/j.jmrt.2021.09.019.
9. W. D. Li, D. Xie, D. Y. Li, Y. Zhang, Y. F. Gao, and P. K. Liaw, *Prog. Mater. Sci.* **118** 100777 (2021), https://doi.org/10.1016/j.pmatsci.2021.100777.
10. E. P. George, W. A. Curtin, and C. C. Tasan. *Acta Materialia* **188** 435 (2020), https://doi.org/10.1016/j.actamat.2019.12.015.
11. M. C. Gao, J.-W. Yeh, P. K. Liaw, and Y. Zhang, *High-entropy Alloys: Fundamentals and Applications*, New York, Springer Publishing Co. (2016), https://doi.org/10.1007/978-3-319-27013-5.
12. O. N. Senkov, D. B. Miracle, K. J. Chaput, and J.-P. Couzinie. *Journal of materials research* **33** 3092 (2018), https://doi.org/10.1557/jmr.2018.153.
13. M. Dada, P. Popoola, and N. Mathe, *World Journal of Engineering* (2021), http://dx.doi.org/10.1108/WJE-01-2021-0040.
14. E. Pickering, A. Carruther, P. Barron, S. Middleburgh, D. Armstrong, and A. Gandy, *Entropy* **23** 98 (2021), https://doi.org/10.3390/e23010098.
15. B. Gludovatz, A. Hohenwarter, D. Catoor, E. H. Chang, E. P. George, and R. O. Ritchie, *Science* **345** 1153 (2014), https://doi.org/10.1126/science.1254581.

16. D. Castro, P. Jaeger, A. C. Daptista, and J. P. Oliveira, *Metals* **11** 648 (2021), https://doi.org/10.3390/met11040648.
17. E. D. Tabachnikova, M. A. Laktionova, Y. A. Semerenko, S. E. Shumilin, and A. V. Podolskiy, *Low Temp. Phys.* **43** 1108 (2017), https://doi.org/10.1063/1.5004457.
18. T. V. Hryhorova, S. E. Shumilin, Y. O. Shapovalov, Y. O. Semerenko, O. D. Tabachnikova, M. A. Tikhonovsky, O. S. Tortika, M. I. Zehetbauer, and E. Schafler, *Journal of V. N. Karazin Kharkiv National University, series "Physics"* **32** 41 (2020), https://doi.org/10.26565/2222-5617-2020-32-05.
19. J. Moon, E. Tabachnikova, S. Shumilin, T. Hryhorova, Y. Estrin, J. Brechtl, P. K. Liaw, W. Wang, K. A. Dahmen, A. Zargaran, J. W. Bae, H.-S. Do, B.-J. Lee, and H. S. Kim, *Materials Today*, in Press, Available online 13 September 2021, https://doi.org/10.1016/j.mattod.2021.08.001.
20. B. Cantor, *Progress in Materials Science* **120** 100754 (2021), https://doi.org/10.1016/j.pmatsci.2020.100754.
21. N. Stepanov, M. Tikhonovsky, N. Yurchenko, D. Zyabkin, M. Klimova, S. Zherebtsov, G. Salishchev, and A. Efimov, *Intermetallics* **59** 8 (2015), https://doi.org/10.1016/j.intermet.2014.12.004.
22. G. A. Salishchev, M. A. Tikhonovsky, D. G. Shaisultanov, N. D. Stepanov, A. V. Kuznetsov, I. V. Kolodiy, A. S. Tortika, and O. N. Senkov, *Journal of Alloys and Compounds* **591** 11 (2014), https://doi.org/10.1016/j.jallcom.2013.12.210.
23. N. D. Stepanov, D. G. Shaysultanov, G. A. Salishchev, M. A. Tikhonovsky, E. E. Oleynik, A. S. Tortika , and O. N. Senkov, *Journal of Alloys and Compounds* 628 170 (2015), https://doi.org/10.1016/j.jallcom.2014.12.157.
24. D. G. Shaysultanov, N. D. Stepanov, G. A. Salishchev, and M. A. Tikhonovsky, *Physics of Metals and Metallography*, **118** 579 (2017), http://dx.doi.org/10.1134/S0031918X17060084.
25. E. D. Tabachnikova, A. V. Podolskiy, M. O. Laktionova, N. A. Bereznaia, M. A. Tikhonovsky, and A. S. Tortika, *J.Alloys Comp.* **698** 501 (2017), https://doi.org/10.1016/j.jallcom.2016.12.154.
26. N. D. Stepanov, N. Yu. Yurchenko, M. A. Tikhonovsky, and G. A. Salishchev; *J. Alloy. Compd.* **687** 59 (2016), http://dx.doi.org/10.1016%2Fj.jallcom.2016.06.103.
27. N. D. Stepanov, D. G. Shaysultanov, R. S. Chernichenko, N. Yu. Yurchenko, S. V. Zherebtsov, M. A. Tikhonovsky, and G. A. Salishchev, *Journal of Alloys and Compounds* **693** 394 (2017), https://doi.org/10.1016/j.jallcom.2016.09.208.
28. B. Schuh, F. Mendez-Martin, B. Volker, E. P. George, H. Clemens, R. Pippan, and A. Hohenwarter, *Acta Mater.* **96** 258 (2015), https://doi.org/10.1016/j.actamat.2015.06.025.

29. A. V. Podolskiy, Y. Shapovalov, E. D. Tabachnikova, A. S. Tortika, M. A. Tikhonovsky, B. Joni, E. Odor, T. Ungar, S. Maier, C. Rentenberger, M. Zehetbauer, and E. Schafler, *Adv. Eng. Mater.* **22** 1900752 (2020), https://doi.org/10.1002/adem.201900752.

30. J. Moon, Y. Qi, E. Tabachnikova, Y. Estrin, W.-M. Choi, S.-H. Joo, B.-J. Lee, A. Podolskiy, M. Tikhonovsky, and H.S. Kim, *Sci. Rep.* **8** 11074 (2018), https://doi.org/10.1038/s41598-018-29446.

31. T. Huang, L. Jiang, C. Zhang, H. Jiang, Y. P. Lu, and T. J. Li, *Sci China Tech Sci.* **61** 117 (2018), https://doi.org/10.1007/s11431-017-9134-6.

32. X. W. Liu, L. Liu, G. Liu, X. X. Wu, D. H. Lu, J. Q. Yao, W. M. Lang, Z. T. Fan, and W. B. Zhang, *Metallurgical and Materials Transactions* (2018), http://dx.doi.org/10.1007/s11661-018-4549-8.

33. L. J. Zhang, P. F. Yu, J. T. Fan, M. D. Zhang, C. Z. Zhang, H. Z. Cui, and G. Li, *Materials Science and Engineering: A* **796** 140065 (2020), https://doi.org/10.1016/j.msea.2020.140065.

34. A. V. Podolskiy, C. Mangler, E. Schafler, E. D. Tabachnikova, and M. J. Zehetbauer, *J. Mater. Sci.* **48** 4689 (2013), https://dx.doi.org/10.1007/s10853-013-7276-y.

35. H. Shahmir, E. Tabachnikova, A. Podolskiy, M. Tikhonovsky, and T. G. Langdon, *J Mater Sci* **53** 11813 (2018), https://link.springer.com/article/10.1007%2Fs10853-018-2456-4.

36. Y. Y. Shang, Y. Wu, J. Y. He, X. Y. Zhu, S. F. Liu, H. L. Huang, K. An, Y. Chen, S. H. Jiang, H. Wang, X. J. Liu, and Z. P. Lu, *Intermetallics* **106** 77 (2019), https://doi.org/10.1016/j.intermet.2018.12.009.

37. M. Y. He, Y. F. Shen, N. Jia, and P. K. Liaw, *Applied materials today* **25** 101162 (2021), https://doi.org/101016/japmt.2021.101162.

38. T. Z. Khan, T. Kirk, G. Vazquez, P. Singh, A. V. Smirnov, D. D. Johnson, K. Yousse, R. Arróyave, *Acta Materialia* **224** 117472 (2021), https://doi.org/10.1016/j.actamat.2021.117472.

39. R. Pippan, S. Scherian, A. Hohenwarter, and M. Hafok, *Mater. Sci. Forum* **584–586** 16 (2008), https://doi.org/10.40 28/www.scientific.net/MSF.584-586.16.

40. G. K. Williamson and W. H. Hall, *Acta Metallurgica* **1** 22 (1953), https://doi.org/10.1016/0001-6160(53)90006-6.

41. G. K. Williamson and R. E. Smallman, *The Philosophical Magazine: A Journal of Theoretical Experimental and Applied Physics* 1 34 (1956), https://doi.org/10.1080/14786435608238074.

42. B. Ya. Farber, N. S. Sidorov, V. I. Kulakov, Yu. A. Iunin, A. N. Izotov, G. A. Emel'chenko, V. S. Bobrov, L. S. Fomenko, V. D. Natsik, and S. V. Lubenets, *Superconductivity* **4** 2394 (1991).

43. A. I. Somov and M. A. Tikhonovsky, *Eutectic composites*. M., Metallurgia (1975) (In Russian).

44. M. A. Tikhonovsky, A. S. Tortika, I. V. Kolodiy, P. I. Stoev, T. Y. Rudycheva, N. S. Berezhnaya, and I. G. Tantsjura, *Probl Atom Sci Tech* **4** 37 (2016).

45. R. E. Smallman and K. H. Westmacott, *The Philosophical Magazine: A Journal of Theoretical Experimental and Applied Physics* 2 669 (1957), https://doi.org/10.1080/14786435708242709.

46. H. V. Rusakova, L. S. Fomenko, S. N. Smirnov, A. V. Podolskiy, Y. O. Shapovalov, E. D. Tabachnikova, M. A. Tikhonovsky, A. V. Levenets, M. J. Zehetbauer, and E. Schafler, *Mat. Sc. and Eng. A* **828** 142116 (2021), https://doi.org/10.1016/j.msea.2021.142116.

47. I. F. Kislyak, K. V. Kutniy, V. S. Okovit, M. A. Tikhonovsky, P. A. Khaimovich, I. V. Kolodiy, and A. S. Kalchenko, *Probl Atom Sci Tech* **2** 109 (2018).

48. W. Woo, M. Naeem, J.-S. Jeong, C.-M. Lee, S. Harjo, T. Kaasaki, H. He, and X. L. Wang, *Materials Science and Engineering: A* **781** 139224 (2020), https://doi.org/10.1016/j.msea.2020.139224.

49. Z. Wu, C. M. Parish, H. Bei, *J. of Alloys and Compounds* **647** 815 (2015), http://dx.doi.org/10.1016/j.jallcom.2015.05.224.

Figures and tables

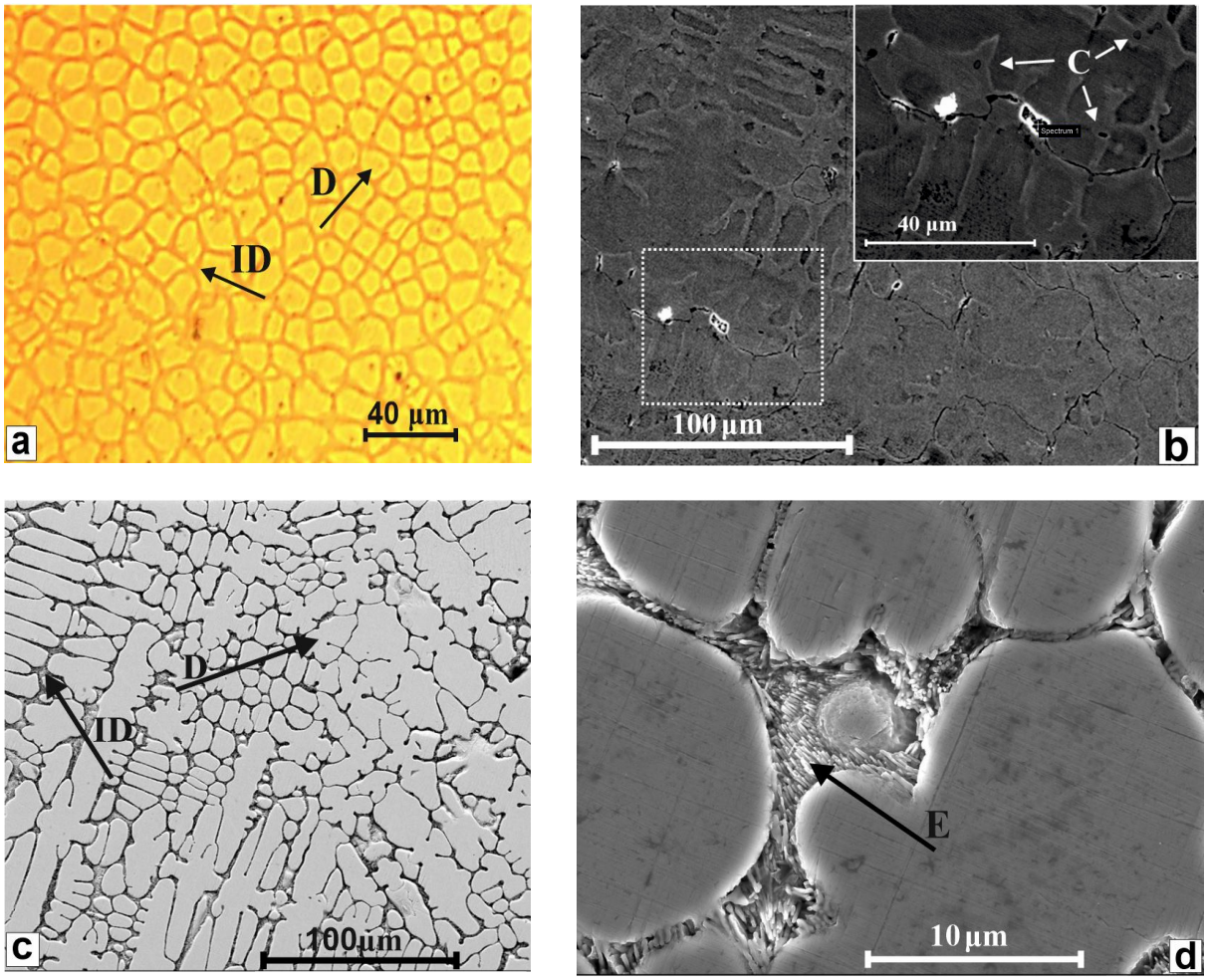

Fig. 1. Structure of the as-cast alloys with different carbon content, at. %: a – 0, b – 1, c, d – 3.

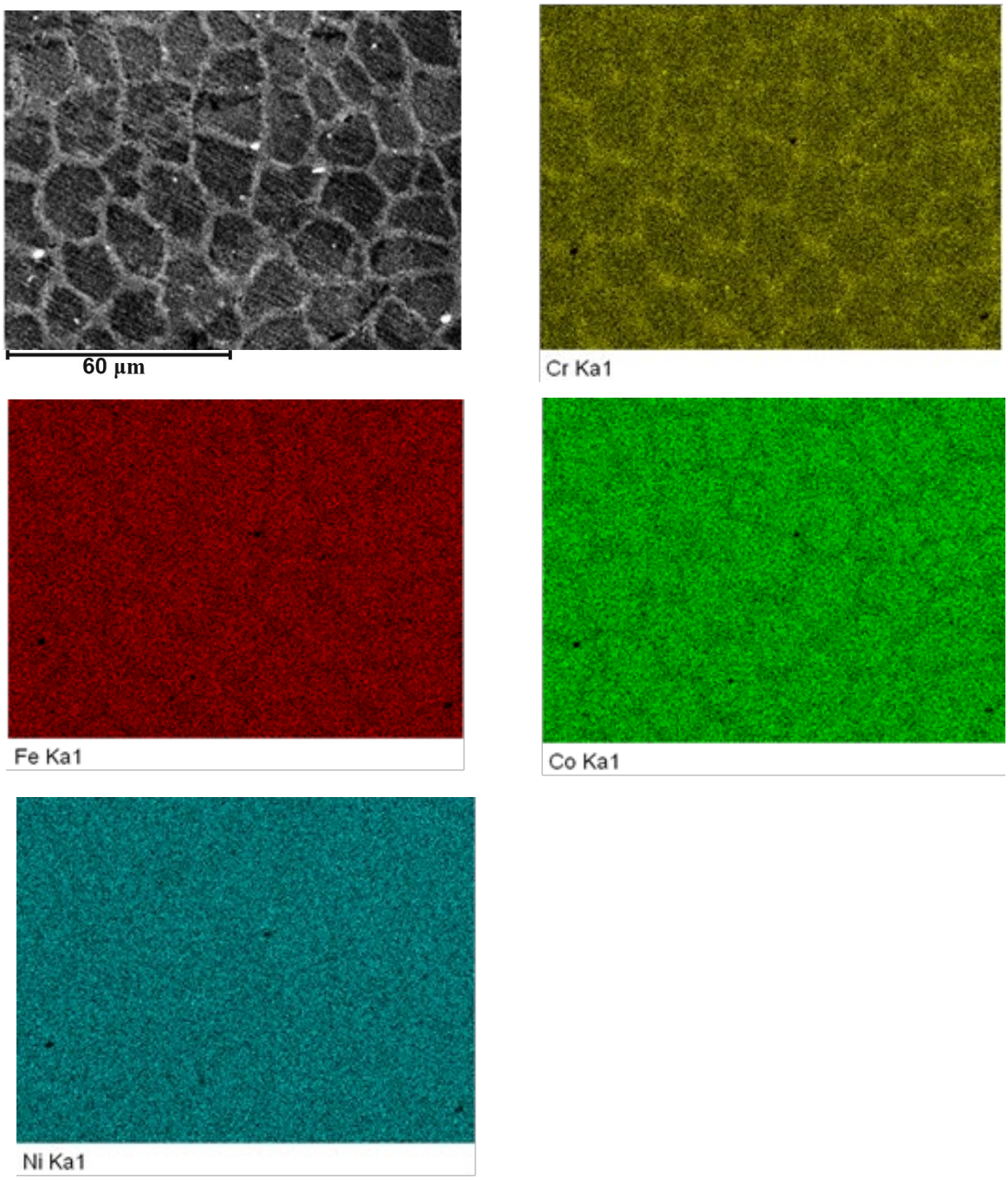

Fig. 2. The EDS elemental maps of the alloy without carbon (C0N0).

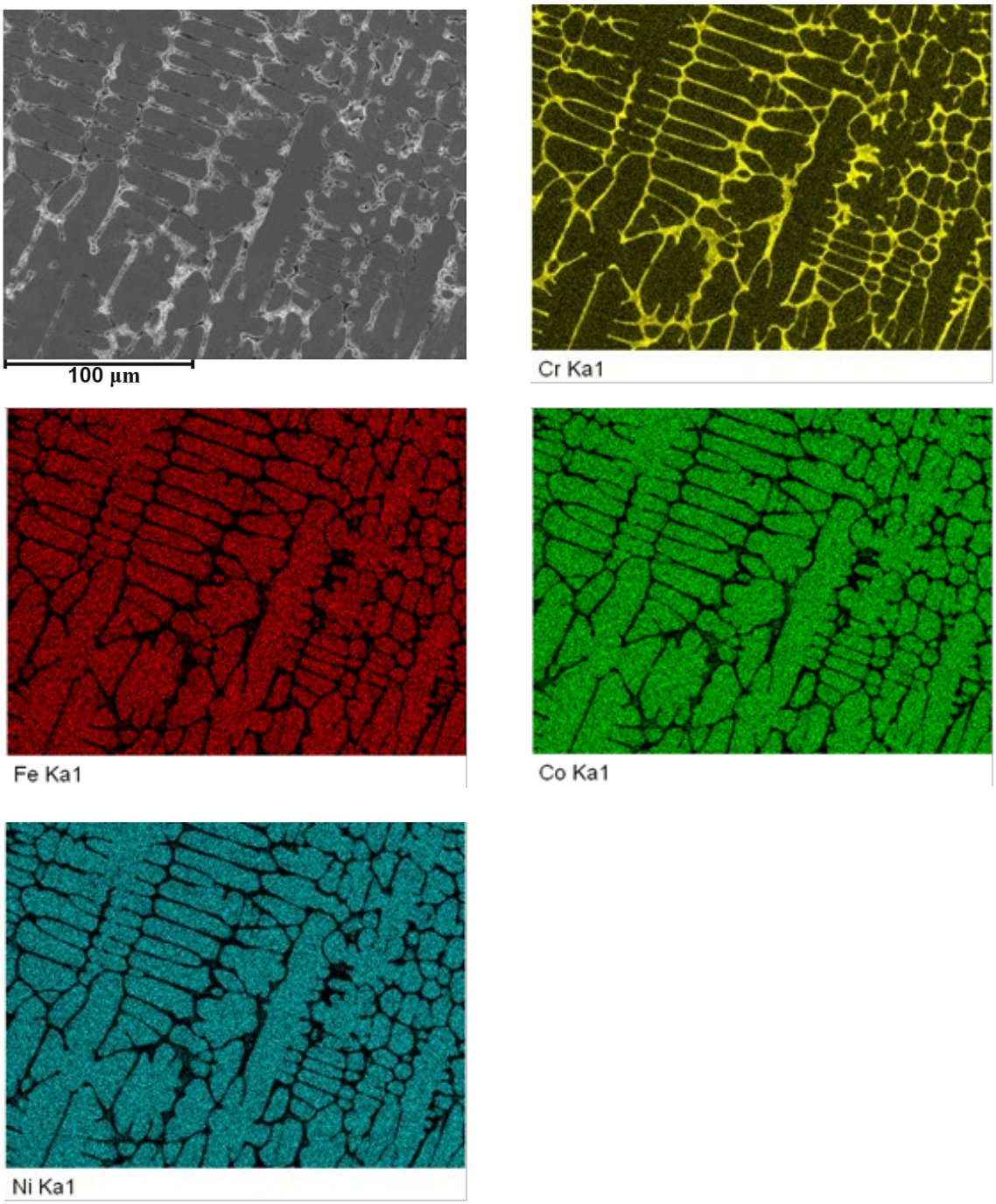

Fig. 3. The EDS elemental maps of the alloy with 3 at. % carbon (C3N0).

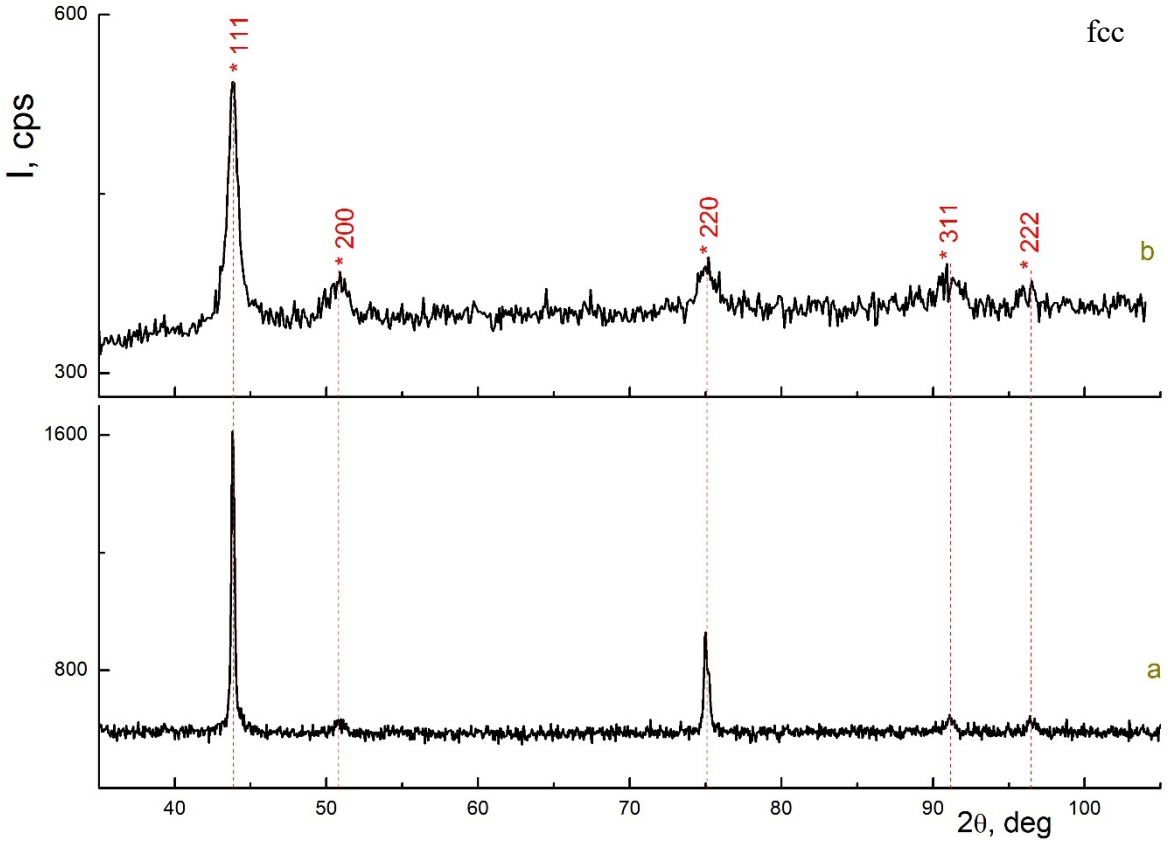

Fig. 4. Diffractograms of the alloy with 3 at. % carbon (C3N0): a – as-cast state, b – after HPT by one revolution (C3N1).

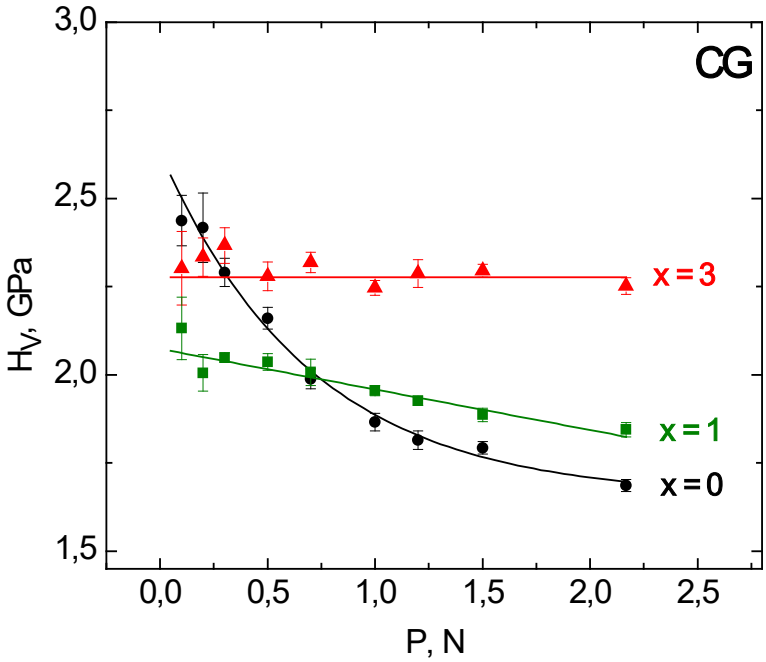

Fig. 5. Microhardness H_V depending on the indentation load P of the CG $Co_{25-x}Cr_{25}Fe_{25}Ni_{25}C_x$ (x = 0; 1; 3) alloys; T = 295 K, loading time t = 10 s. Each point – 10 marks-average microhardness. Error bar size – mean square deviation for the average value of microhardness.

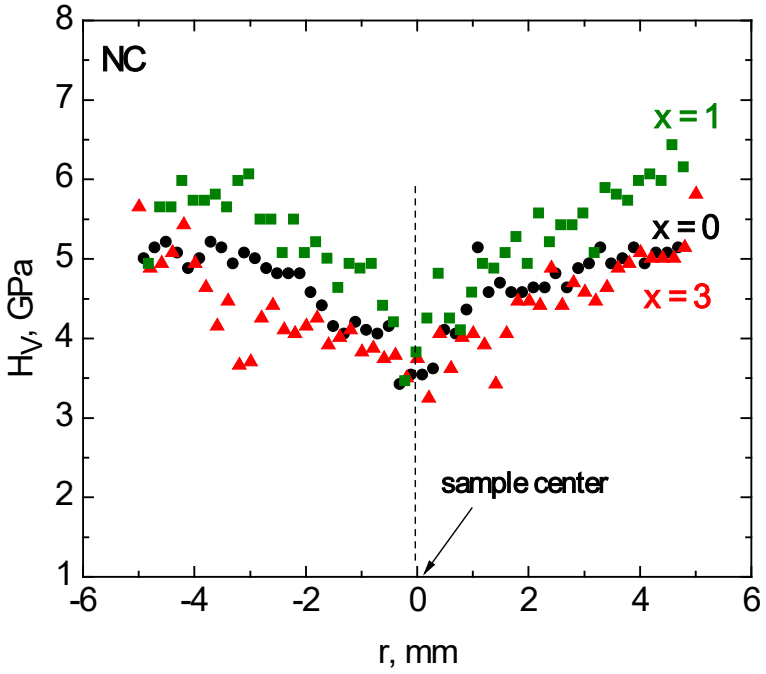

Fig. 6. Microhardness H_V depending on the distance from the disk center r of the samples with different carbon concentration, subjected to torsion for $N = 1$; $P = 1.5$ H, $t = 10$ c, $T = 295$ K, spacing of indents is 200 μm. Each point corresponds to the microhardness value calculated from one indentation.

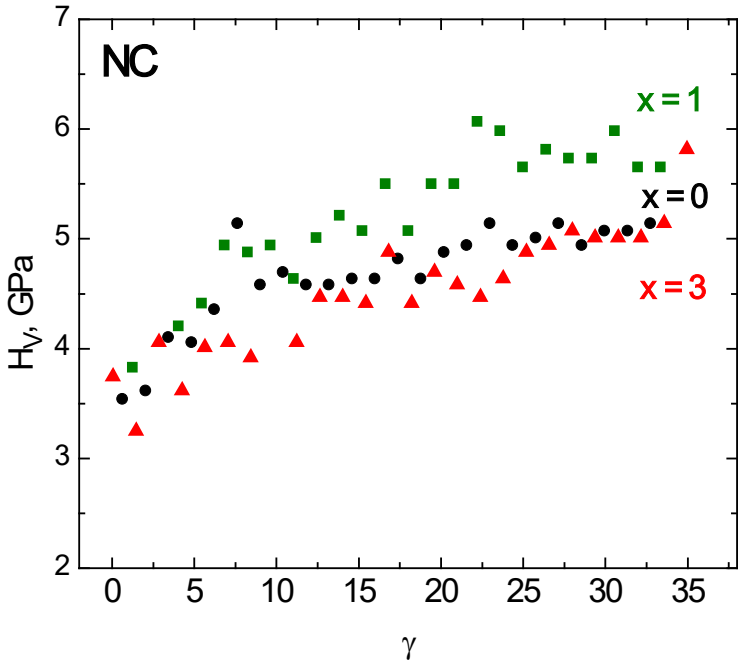

Fig. 7. Microhardness H_V depending on the shear strain γ (calculated from the data in Figure 6).

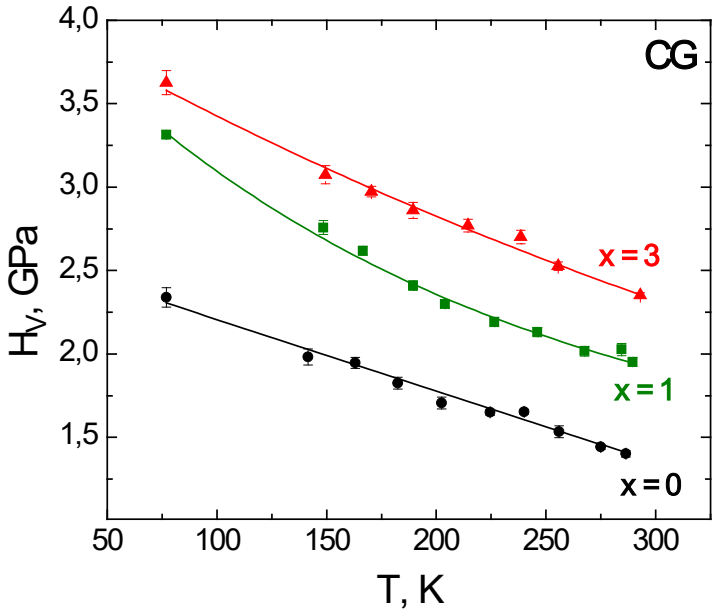

Fig. 8. Temperature dependence of microhardness of as-cast CG samples. Each point on the graph is the average of 10 indents. t = 10 s, P = 2.2 N.

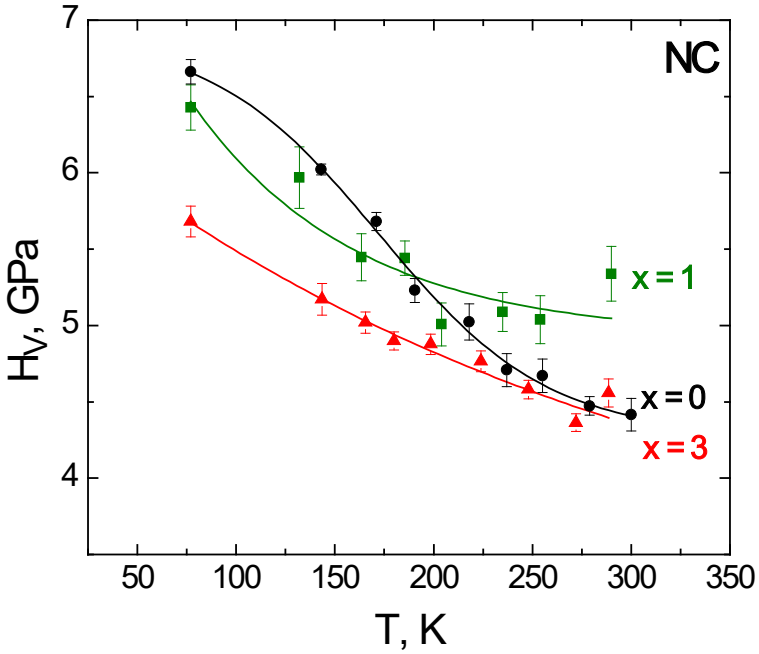

Fig. 9. Temperature dependence of microhardness of NC samples. Each point on the graph is the average of 10 indents. t = 10 s, P = 2.2 N.

Table 1. Concentration of the metallic elements in the dendrites (D) and interdendritic regions (ID)

Alloy / Element concentration, at.%	Co	Cr	Fe	Ni
C0				
D	25.96±0.07	24.56±0.06	25.06±0.07	24.43±0.07
ID	23.18±0.70	28.10±1.34	24.21±1.01	24.51±0.14
C1				
D	25.86±0.01	23.91±0,06	25.86±0.01	23.78±0.15
ID	23.91±0,06	28.53 ±0.13	24.60±0.10	26.91±0.08
C3				
D	23.61±0.05	23.03±0.03	25.60±0.09	26.91±0.08
ID (eutectic)	15.25±0.44	50.77±1.20	19.20±0.20	14.76±0.57

Table 2. Lattice parameters and substructural parameters of fcc phase in the HPT sample

Sample	Lattice parameter *a*, Å	SFC α	Crystallite size *D*, nm	Microstrains level ε	Dislocation density ρ, m^{-2}
C0N0	3.580	0.0344	40.9	1.47×10^{-3}	1.07×10^{15}
C1N1	3.588	0.0423	32.6	1.66×10^{-3}	1.5×10^{15}
C3N1	3.585	0.0354	49.4	1.62×10^{-3}	9.8×10^{14}

Структура та низькотемпературні мікромеханічні властивості литих та підданих ІПД високоентропійних сплавів $Co_{25-x}Cr_{25}Fe_{25}Ni_{25}C_x$

А. В. Левенець, Г. В. Русакова, Л. С. Фоменко, Yi Huang, І. В. Колодій, Р. Л. Василенко, О. Д. Табачникова, М. А. Тихоновський, T.G. Langdon

Досліджено вплив домішок вуглецю на структуру та механічні властивості високоентропійних сплавів $Co_{25-x}Cr_{25}Fe_{25}Ni_{25}C_x$ (x = 0, 1, 3, ат. %) в двох структурних станах, литому крупнозернистому (КЗ) і нанокристалічному (НК), отриманому інтенсивною пластичною деформацією (ІПД). ІПД здійснювалася методом крутіння під високим тиском при кімнатній температурі. Механічні властивості досліджувалися методом мікроіндентування в інтервалі температур T = 77-300 К. Установлено, що в литому стані всі сплави мають дендритну мікроструктуру та неоднорідний розподіл елементів. При x = 0 і x = 1 дендрити збагачені залізом і нікелем, а міждендритні зони – хромом. При x = 3 у міждендритних зонах формується евтектика, яка складається з багатокомпонентної матриці та тонкодисперсних евтектичних дендритів карбіду M_7C_3, де M – переважно хром. Основна фаза в сплавах має ГЦК ґратку, при цьому розчинність вуглецю в ній складає близько 1 ат. %. ІПД приводить до ефективного подрібнення мікроструктури (розмір зон когерентного розсіяння складає близько 30-50 нм), збільшення густини дислокацій до $1\text{-}1{,}5\cdot10^{15}$ $м^{-2}$ та зростання концентрації дефектів пакування. Мікротвердість КЗ сплавів при кімнатній температурі зі збільшенням концентрації вуглецю монотонно зростає, тоді як в НК сплавах максимум мікротвердості H_V досягається при 1 ат. % вуглецю. Причиною такої аномальної поведінки мікротвердості НК сплавів є збільшення розміру зерна та зменшення густини дислокацій в сплаві з x = 3 порівняно зі сплавом з x = 1. При зниженні температури від кімнатної до температурі рідкого азоту мікротвердість КЗ і НК сплавів зростає приблизно в 1,5-1,7 та 1,2-1,5 рази відповідно, що свідчить про термоактивований характер пластичної деформації під індентором. Отримані результати вказують на те, що основну роль у зміцненні КЗ сплавів $Co_{25-x}Cr_{25}Fe_{25}Ni_{25}C_x$ грають твердорозчинне та дисперсійне зміцнення, тоді як в НК сплавах – зміцнення, обумовлене зменшенням розміру зерна (згідно із співвідношенням Холла-Петча) та збільшенням густини дислокацій (згідно із співвідношенням Тейлора).

Ключові слова: високоентропійні сплави, легування вуглецем, мікроструктура, мікротвердість, інтенсивна пластична деформація, механізми деформації.